Spectrochimica Acta Part A: Molecular and Biomolecular Spectroscopy 280 (2022) 121504

Contents lists available at ScienceDirect

Spectrochimica Acta Part A:
Molecular and Biomolecular Spectroscopy

journal homepage: www.journals.elsevier.com/spectrochimica-acta-part-a-molecular-and-biomolecular-spectroscopy

Open-source mobile multispectral imaging system and its applications in biological sample sensing

Fuzhou Shen, Hancheng Deng, Lejun Yu *, Fuhong Cai *

Mechanical and Electrical Engineering College School of Biomedical Engineering, Key Laboratory of Biomedical Engineering of Hainan Province, One Health Institute, Hainan University, Haikou 570228, China

HIGHLIGHTS

- An open-source mobile multispectral imaging system was developed with multi-band (36 kinds of) LEDs and an industrial imaging system to obtain sufficient spectral data for biomolecular analysis while ensuring high spatial resolution.
- All the LEDs were switched on sequentially via a program to obtain multispectral imaging data without spatial scanning.
- The self-contained system can be applied for in-situ nondestructive biological sample sensing, such as meat freshness analysis, in-vivo tumor imaging in mice and chlorophyll spatial distribution imaging.
- Combining multispectral image data with SVM algorithm to realize meat freshness classification.

GRAPHICAL ABSTRACT

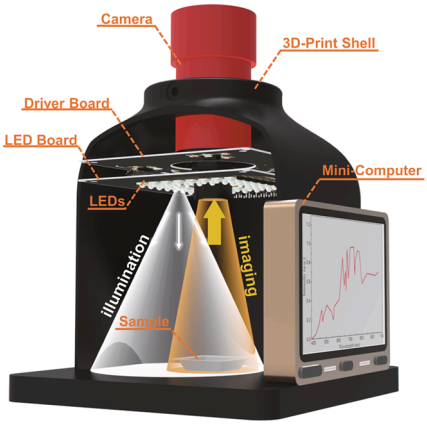

ARTICLE INFO

Keywords:
LED matrix
Multi-spectral imaging
Biological sample sensing

ABSTRACT

Visible-near-infrared spectroscopy data can be utilized as an important quantitative indicator of biomolecular quantitative analysis. When acquiring spectral information, hyperspectral/multispectral imaging systems can obtain the spatial information of the object of interest. This allows the complete spatial–spectral information of the object of interest to be acquired and the spatial distribution of biomolecules to be analyzed. In this study, we present an open-source mobile multispectral imaging system, test the influence of the utilization of LEDs on the multispectral image, and design image-processing algorithms to correct this influence. To demonstrate the effectiveness of the system, the system is applied to meat freshness analysis, small-animal tumor *in-vivo* imaging, and chlorophyll spatial distribution imaging. The experimental results verify that our system has stable performance and is compatible with a wide range of spectral imaging applications.

* Corresponding authors.

https://doi.org/10.1016/j.saa.2022.121504
Received 22 March 2022; Received in revised form 10 June 2022; Accepted 12 June 2022
Available online 15 June 2022

1. Introduction

In recent years, machine vision technology has attracted much attention. Relying on high-performance photoelectric instruments and highly intelligent and automatic image-processing algorithms, machine vision has been widely used in scientific research and industrial settings. Additionally, there is an increasing interest in studying hyperspectral/multispectral cameras for biological sensing and identification[1–4]. Compared with the monochrome or RGB cameras used in traditional machine vision, hyperspectral/multispectral cameras can synchronously obtain the spatial optical information as well as the spectral data, which serves as an important link between biomolecular chemical properties and quantitative data[5,6]. For example, using the unique spectral data of chlorophyll[7–9], the type, growth, and distribution of vegetation can be analyzed. Hyperspectral systems usually acquire much more spectral information than multispectral systems and it is widely believed they will eventually replace multispectral systems.

To obtain the spatial–spectral data, hyperspectral cameras usually utilize a complex diffraction (or refraction) spectroscopic system and a spatial or spectral scanning module to capture a hyperspectral cube [10–13].

A spectral scan spectrometer adopts a tunable filter as the spectroscopic element, such as a liquid crystal tunable filter and acousto-optic tunable filter[14–16]. The spatial information of an object at a certain wavelength can be accessed by fixing the tunable filter between a complementary metal–oxide semiconductor (CMOS) and the imaging lens. The spatial resolution of this system is high, and the optical structure is easy to build. However, this type of spectrometer is more expensive. The spectral resolution and detection efficiency are not yet comparable to those of a grating spectrometer.

Unlike the spectral scan method, the spectroscopic elements of a spatial scan spectrometer[17–19] primarily include the prism and grating. It obtains the spectral data on one point or one line of the object at a time and synthesizes them into image data[20]. For example, in a push-broom system, the light of an object successively passes through the slit and spectroscopic system into monochromatic light that expands with wavelength. A hyperspectral cube can be accessed by pushing the entire field of view mechanically. However, mechanical scanning components can cause problems, such as slow imaging speed and low spatial resolution, which restrict the application of hyperspectral cameras.

From the perspective of spectral analysis, a large number of spectral band data do not need to be obtained in some applications. For example, in a study on the detection of vegetation chlorophyll[21,22], with the help of the red edge effect, only 3–5 spectral bands were required to analyze the vegetation. In another study on blood oxygen saturation [23,24], the ratio of oxyhemoglobin (HbO_2) to total hemoglobin was calculated by using three characteristic spectral bands: the green, red, and infrared bands. In a study for predicting the sugar content of fruit [25], such as apples, four optimal wavelengths (461, 469, 947, and 1049 nm) were used. As can be seen from the abovementioned examples, we do not need redundant spectral data for spectral data analysis. Therefore, if appropriate light sources are selected for specific applications, the detection of specific biomolecules can be completed without the need for hyperspectral data.

Compared with hyperspectral imaging systems, the major advantages of multispectral imaging systems are their high temporal–spatial resolution and the simplicity of data post-processing. In recent years, the light-emitting diode (LED) industry has been developing rapidly[26]. LEDs have the characteristics of small structure, high photoelectric conversion efficiency, and strong illumination, and their spectral range can cover 400–1100 nm, which is the same as the spectral range of a traditional hyperspectral camera. By using LEDs with different wavelengths to illuminate the sample, we can obtain the multispectral information of the object without a diffraction module or scanning module. Although some LED-based multispectral cameras have been studied in the literature[27,28], these previous studies used a small number of LEDs and were developed for specific individual applications; they lack systematic considerations in terms of lamp density, illumination uniformity, and imaging time.

In our study, we propose the use of multi-band (36 kinds of) LEDs and an industrial imaging system to obtain sufficient spectral data for biomolecular analysis while ensuring high spatial resolution. Owing to the compact structure size of LEDs, the size of the multi-band LEDs integrating 36 different-band LEDs and corresponding electrical drivers was 96 mm × 96 mm × 115 mm. The electrical power for each LED was 3 W[29,30], which can ensure sufficient lighting intensity. The system can be controlled through the serial port and realize spectral scanning and synchronous spatial imaging. In addition, to improve system integration, we designed a corresponding fixture and shell, and manufactured the prototype through 3D printing.

2. Materials and methods

Fig. 1 shows a schematic of the proposed mobile multispectral imaging system. The entire photoelectric system was housed in a self-contained package, which contained an imaging unit, illumination unit, and control unit. This imaging system enclosure case was fabricated via 3D printing and had preset slots for positioning all the units. These units enable our system to perform *in-situ* spectral imaging experiments.

A sample was placed right under the imaging lens, which was illuminated by LEDs. Each LED was switched on sequentially via a program. The images in each band were collected by a high-resolution camera in synchronization and post processing involved stacking the images to obtain a multispectral data cube. The result was displayed on the screen of a mini-computer.

The main components of the illumination unit were the LED matrix and its driving circuit. There were 36 LED chips (3535 package chip, i.e., the size of the chip was 3.5 mm × 3.5 mm) with different wavelengths housed as a LED matrix, which played an essential role in multispectral lighting. The spectral range, spectral resolution, and illumination intensity were determined by these 36 LED chips. The rated electrical power of each LED chip was 3 W. The constant current chip (PowTech's PT4205) was selected as the LED driver chip because of its 97 % peak power conversion efficiency and the 3 % current accuracy, which can ensure the stability of the light source output.

The core of the control unit was the switching control of the LEDs and interaction with the host computer. A single-chip microcomputer was used to change the conduction mode of the metal–oxide–semiconductor field effect transistor (MOSFET), which further controlled the switching state of the LEDs. Based on these electronic devices, each LED could be switched on and off via a program.

As shown in Fig. 1(c), the LED chips covered spectral range from 380 to 1000 nm, and their central wavelengths and corresponding optical power are listed in Table 1. In the spectral range of 400–500 nm, the average full width at half maximum (FWHM) height of the optical spectrum for each LED was approximately 22 nm; thus, the spectral resolution in this range can be defined as 22 nm. In the range of 500–600 nm, because we can purchase fewer types of LED chips (only 6 chips in this spectral range), the spectral resolution was approximately 40 nm. Similarly, the spectral resolution was 19, 25, 32, and 73 nm in the 600–700, 700–800, 800–900, and 900–1000 nm range, respectively.

Although all LEDs had the same rated electrical power, their light-emitting power varied significantly owing to the different electro-optical conversion efficiency. For the CMOS chip, photons with different wavelengths resulted in different quantum conversion efficiencies. Therefore, under the same camera capture parameters and electrical power, some LEDs may cause CMOS chip saturation (owing to its relatively strong illumination intensity and the high quantum conversion efficiency of the detector). Correspondingly, to overcome these problems, appropriate exposure times for 36 LEDs with different wavelengths were preset to avoid signal saturation of the CMOS

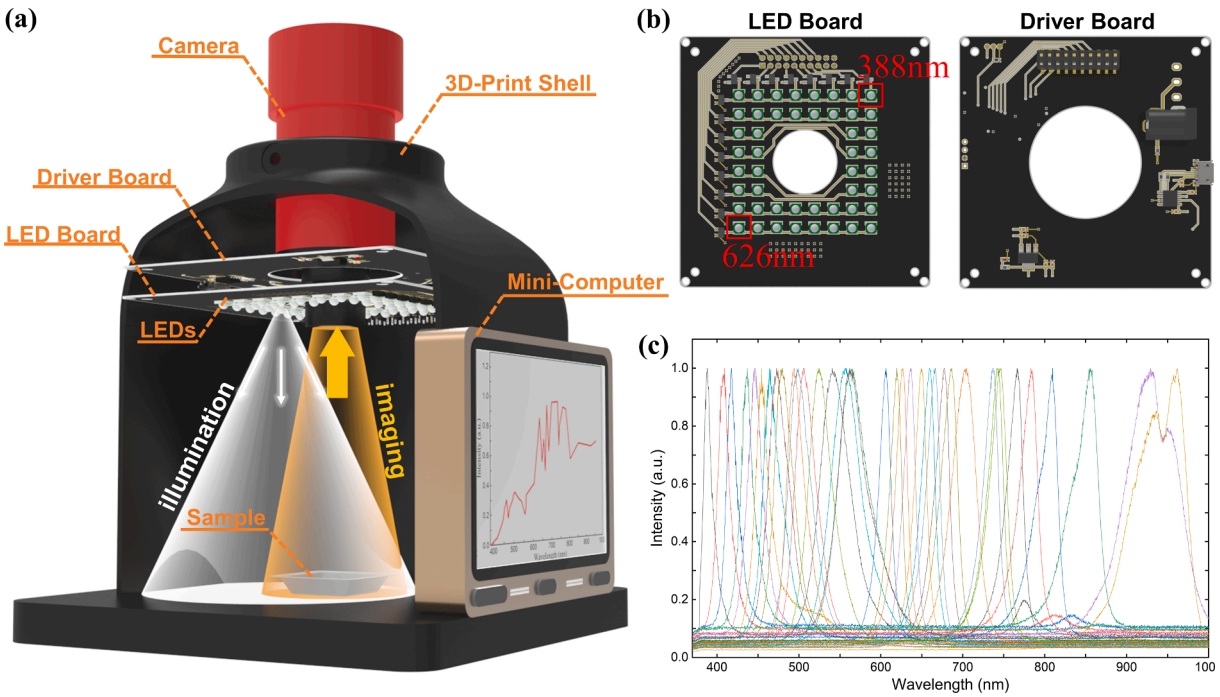

Fig. 1. (a) Structure of the mobile multispectral imaging system. (b) Driver board and the LED board. (c) Optical spectra of the 36 LEDs.

Table 1
The optical power of 36 LEDs and their corresponding camera exposure time during imaging experiments.

Wavelength (nm)	Exposure time(us)	optical power (mw)	Wavelength (nm)	Exposure time(us)	optical power (mw)
388	500	498	619	680	117
409	400	738	626	550	172
417	300	862	636	200	527
436	400	716	649	100	412
446	300	873	659	100	535
454	350	662	666	300	359
464	500	551	676	160	535
472	340	532	686	160	556
479	340	719	703	160	417
494	490	421	736	300	603
499	640	338	743	400	535
505	500	282	746	400	503
524	500	273	766	400	522
540	530	141	783	500	573
557	530	150	808	400	481
562	660	102	855	700	835
564	660	142	931	5000	228
606	1900	225	961	1500	596

cameras. Herein, a standard diffuse whiteboard (99 % reflectivity) was selected as the imaging sample. Under different wavelengths of LED illumination, we adjusted the CMOS exposure time to avoid CMOS overexposure. As the reflectivity of experimental samples is usually lower than 99 %, under these settings, the multispectral images obtained during the experiment will not be saturated. The total exposure time was 21.85 ms for 36 LEDs. Therefore, our system could realize high-speed multispectral imaging without mechanical scanning.

Moreover, uniformity of the illumination was another issue that needed to be addressed. To expand the spectral band, the number of LEDs was increased, which led to a larger circuit board. When LEDs in different positions emitted light, the image nonuniformity was varied. For instance, when a 388-nm LED and a 626-nm LED, whose positions in the circuit board are highlighted in Fig. 1(b), were used for diffuse whiteboard imaging, the results are as shown in Fig. 2(b). There were considerable differences between these two imaging results due to the LED positions. Moreover, as mentioned earlier, to ensure that there is no over-exposure in multispectral images, we adopted different exposure time settings for 36-LED illumination. Owing to this artificial operation, the result was incompatibility between images in different bands.

To overcome these problems, we used the multispectral images of the standard diffuse whiteboard as a reference. The original images obtained in the following experiment were processed by the following algorithm:

$$Processed\ image\ (\lambda) = \frac{Original\ image\ (\lambda)}{Whiteboard\ image\ (\lambda)}$$

where the standard whiteboard image illuminated by the λnm light is denoted as *Whiteboard image* (λ) and the image of any sample illuminated by the λnm light is denoted as *Original image* (λ). The nonuniformity issue can be corrected using this method. In addition, through this processing, each pixel in the *Processed image* (λ) represents the reflectivity at a certain wavelength. Therefore, the incompatibility caused by different exposure times at different wavelengths can be corrected.

3. Experimental results and discussion

3.1. Multispectral imaging and freshness discrimination for meat samples

First, we applied the mobile multispectral imaging system to measure meat freshness. Meat is one of the primary sources of protein. Meat freshness is vital to good health. Using our imaging system, we could realize the nondestructive and high-speed freshness monitoring of meat. In the experiment, we selected pork tenderloin as the imaging sample. The fresh pork tenderloin was removed from connective tissue in the supermarket and cut into 170 slices of roughly uniform size. Each slice weighed approximately 60 g. To minimize the effect of water volatilization on the experimental data, we utilized clingfilm to wrap the samples in Petri dishes and stored them at room temperature (24 °C). The experiment was conducted every 2 h, and 10 slices were used in each iteration. After the acquisition of multispectral images of meat samples, a grinder was used to crush the meat slices for chemical detection. We mixed 5 g of minced meat with 20 ml of distilled water;

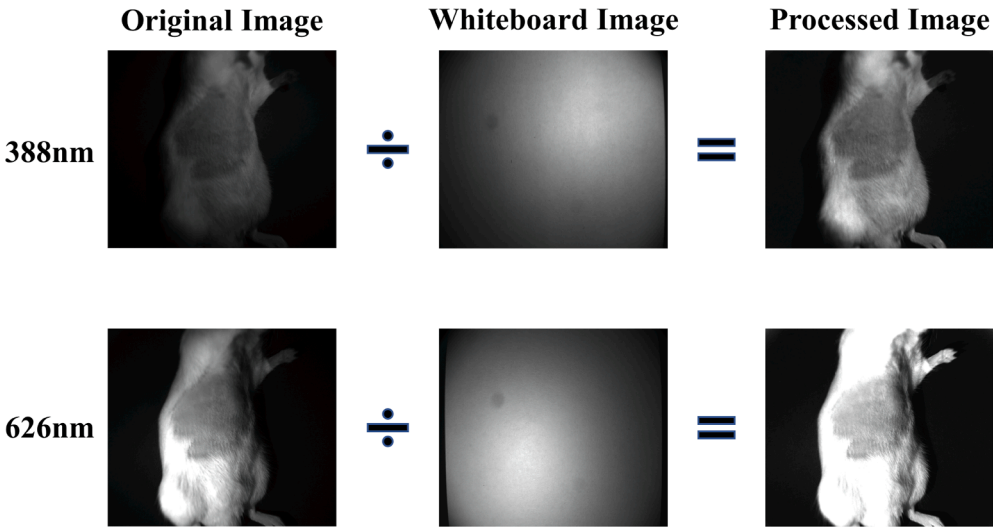

Fig. 2. Original images and processed images corrected by the nonuniformity correction algorithm.

this mixture was allowed to stand for 10 min. The detection tube was shaken well where 2 ml of supernatant and two drops of total volatile basic nitrogen (TVB-N)[31] were mixed in. Subsequently, the mixed solution was compared with the standard color card for semi-quantitative analysis. The operations were repeated three times to obtain the average value. In accordance with the National Standards of China GB2707, the freshness of meat can be divided into three grades according to their TVB-N content: fresh meat (≤15 mg/100 g), semi-rotten meat (≤25 mg/100 g), and fully rotten meat (greater than25 mg/100 g). Fig. 3(b) shows the colors of the detection reagent for three kinds of meat sample.

Based on a standard chemical detection method, the experimental samples of fresh meat, semi-rotten meat, and fully rotten meat were 7, 6, and 4 groups, respectively (10 slices of meat in each group).

Fig. 3(c) illustrates the multispectral imaging results for fresh meat samples. Under the irradiation of the LED matrix, 36 grayscale images were obtained. Under the illumination of short-wavelength LEDs (i.e., 388 and 409 nm), the gray value of the meat sample image was weak because the hemoglobin in the meat had strong absorption for blue light. For the images illuminated by 931 and 961 nm LEDs, the gray value of the image decreased significantly because water had larger absorption for these two spectral bands.

For the image obtained under the irradiation of a single LED, the gray value of each pixel in the image was defined as its reflected light intensity at the LED central wavelength. For a fixed pixel, 36 reflected light intensities at 36 central wavelengths were obtained and formed a reflected spectrum at this corresponding spatial position. The signal-to-noise ratio (SNR) of the reflected spectrum of a single pixel was low, which was not conducive to spectral analysis. Therefore, for one grayscale image, the gray values of all pixels in one region of interest (ROI) were integrated and the mean gray value of the ROI was obtained as the reflected light intensity at one wavelength. When these calculations

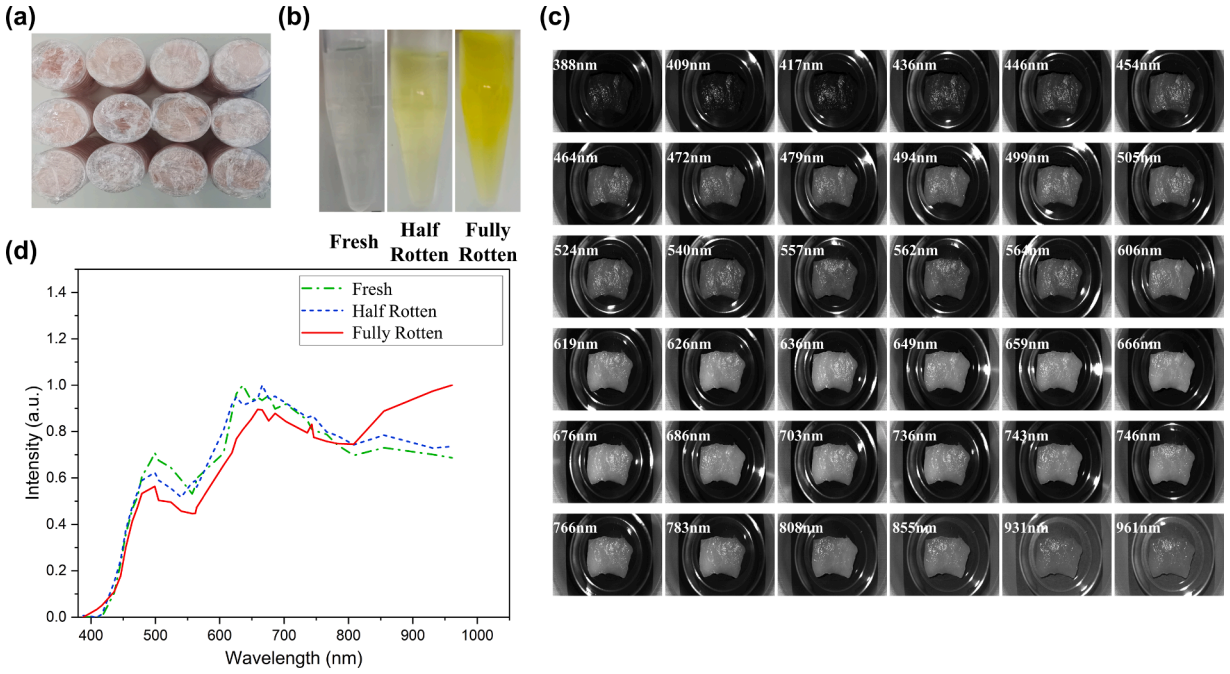

Fig. 3. (a) Meat samples utilized in our work. (b) Result of TVB-N reagent detection. It is obvious that the color of reagent turned yellow as the meat deteriorates. (c) Multispectral imaging results for fresh meat samples. (d) Spectral curves extracted from the multispectral imaging results.

were applied to 36 grayscale images, a reflected spectrum of the ROI with high SNR was acquired.

For each sample, five ROIs were selected to extract reflected spectra. Therefore, there were 850 spectral results in the meat reflected spectral database. The data matrix of the database was set to 170 × 5 × 36, where 170 represents the total number of samples, 5 represents the number of ROIs selected for each sample, and 36 is the number of multispectral camera LEDs. Next, a principal component analysis (PCA) algorithm was applied to reduce the characteristics of data redundancy effectively.

Fig. 4(a) illustrates the dimensionality reduction visualization results after PCA processing. It can be seen that the principal component coordinates of three kinds of meat samples were well distinguished. Further, we chose a support vector machine (SVM) classifier to classify meat freshness. Herein, 70 % of the data (595 values) as the training set and 30 % of the data (255 values) were used as the test set for training and classification. Fig. 4(b) and (c) show the results of linear kernel classification and polynomial kernel classification[32], with an accuracy of approximately 87.8 and 91.8%, respectively. The results demonstrate that the multispectral imaging detection system has great potential in meat freshness detection.

3.2. Multispectral in-vivo imaging for mouse tumor and human hand

A human hand was taken as the sample to collect multispectral images[33]. Fig. 5(a) shows the multispectral images of the fingers and palm, wherein both the fingerprints and palmprints are clearly presented. These results demonstrate the high spatial resolution of our system. The gray value of the image in the blue light band was very low owing to the attenuation caused by oxyhemoglobin (HbO_2) and hemoglobin (Hb), whose absorption spectra are shown in Fig. 5(b). As shown in Fig. 5(c), the two ROIs were selected in the center of the palm and the middle fingertip. The mean reflected spectra can be accessed by superimposing the average gray value of all points in ROIs under the illumination of different wavelengths. The blood concentration at the surface of the fingertip is usually higher than that of the palm and the blood oxygen saturation of healthy people is greater than 90 %. Therefore, owing to the absorption of HbO_2, the reflected spectrum of the fingertip had sharper attenuation in the 500–600 nm band compared with that of the palm.

Additionally, we applied the mobile multispectral imaging system to *in-vivo* tumor imaging. To establish a mouse tumor model more efficiently, we selected BALB/C mice[34] as experimental subjects, the biggest feature of which is that there are no immune organs, such as thymus, and there will be no excessive rejection of exogenous cells. BALB/C female mice at 6–8 weeks were obtained from the Guangdong Medical Laboratory Animal Center. Animal handing procedures were performed following the guidelines of the Regional Ethics Committee for Animal Experiments. To establish the breast tumor model, 2.0 × 10^5 4 T1 cells (mouse breast cancer cells) were subcutaneously implanted into the right breast area of the mice. Tumors developed in approximately 1 week and their size increased over time. There was no spontaneous tumor regression during the entire experiment.

The mice were anesthetized by inhaling 2 % v/v isoflurane and fixed on a black uniform laboratory table with the abdomen facing up as shown in Fig. 6(a). The imaging system was located directly above the mouse and multispectral images of the tumor were acquired on the seventh day after implantation.

Fig. 6(b) illustrates the multispectral imaging results of the mouse on the seventh day. The spatial images were only observed and the information at the biomolecular level could not be extracted. However, if combined with spectral information, we could deeply analyze the tumor area. Owing to the tumor tissue requiring more nutrient supply, the blood vessels in this region were relatively denser and the hemoglobin concentration was higher than normal tissue. To obtain the reflected spectrum of tumor tissue, an ROI was set at the tumor area of the mouse and the corresponding reflected spectrum is demonstrated in Fig. 6(c). As a reference, the reflected spectrum of normal tissue was extracted and plotted in Fig. 6(c). In these two reflected spectra, the amplitude in reflective light of 400–600 nm from tumor tissue was significantly lower than that of normal tissue. This confirms that the tumor tissue has more dense vascular density. These characteristics can be used for tumor region localization. Because the tumor tissue absorbed more 400–600 nm (visible) spectral light, the gray value of the visible images of the tumor area should be lower than that of the near-infrared images. We can calculate the ratio of infrared wavelength image to visible light image. Because the tumor had a large absorption at visible light, the tumor area in the ratio image should exhibit a larger amplitude, which is the average image of 600–650 nm divided into that of 500–550 nm.

3.3. Multispectral imaging for a plant leaf

Furthermore, we applied the system to perform multispectral imaging for a plant leaf. We selected a leaf that appeared yellow as the imaging sample, and the imaging results are shown in Fig. 7(a). On account of the abundant chlorophyll in the leaf, which had strong absorption in the blue band (the chlorophyll absorption spectrum shown in Fig. 7(b) exhibits a strong absorption peak around the 400 nm band), the gray value of the images was extremely low under the illumination of short-wavelength LED (i.e., 388, 409, 417, 436, 446, and 454 nm). Chlorophyll exhibited strong absorption for red light around the 670 nm band. As the wavelength gradually redshifted, the gray value of the image increased and reached a maximum value in the near-infrared spectral region of 680–800 nm, which is noted as the red edge effect.

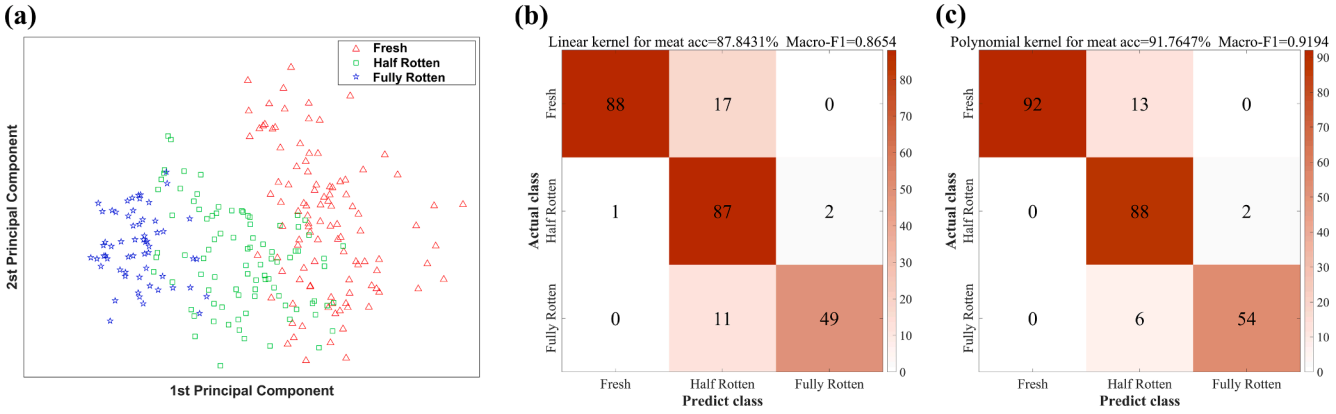

Fig. 4. (a) Relationship between PC1 and PC2 of three states of meat. (b) Linear kernel classification results of the three states of meat. (c) Polynomial kernel classification results of three states of meat.

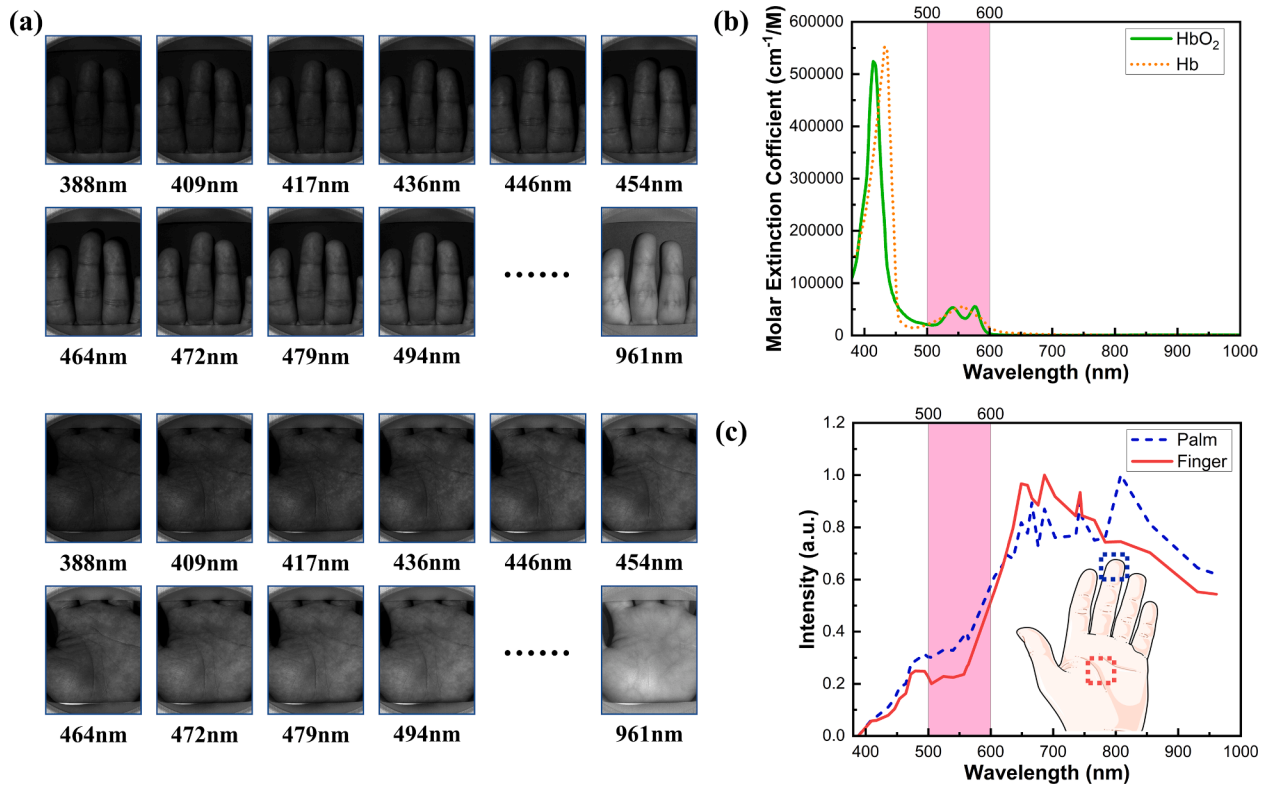

Fig. 5. (a) Multispectral images of the fingers and palm. (b) Absorption spectra of HbO_2 and Hb. (c) Mean reflected spectra of the palm and the middle fingertip accessed by superimposing the average gray value of all points in the blue region or red region.

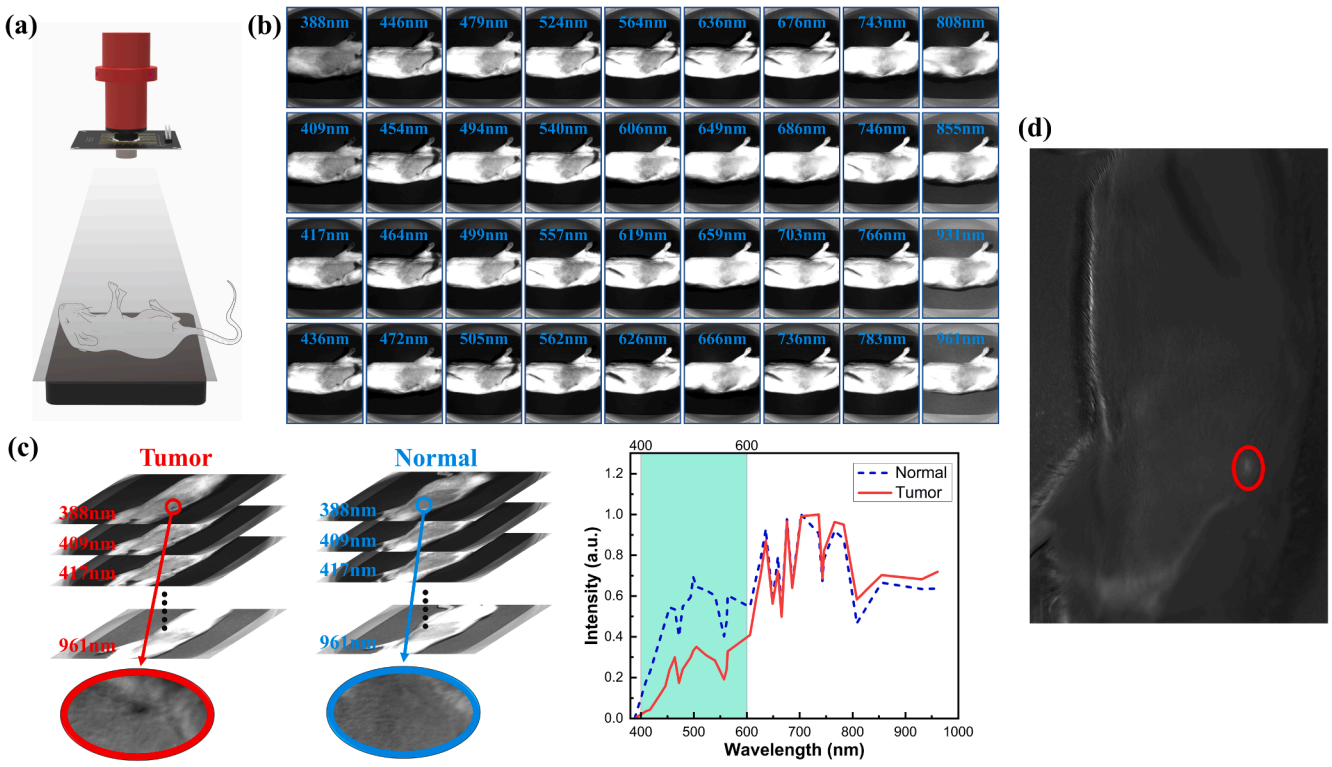

Fig. 6. (a) Schematic diagram of the *in-vivo* imaging experiment. (b) Multispectral images accessed on the seventh day. (c) Reflected spectra of tumor and normal tissue. (d) Processed image for tumor localization.

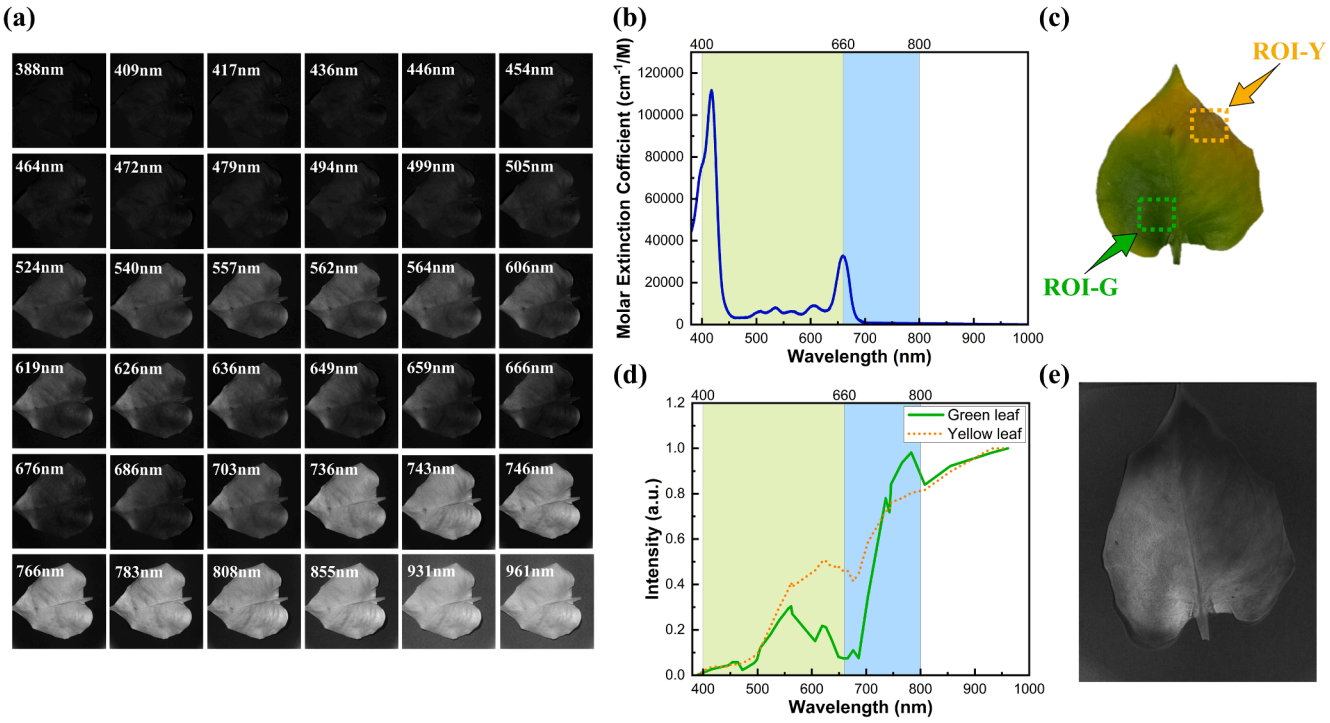

Fig. 7. (a) Imaging results of the leaf under 36-LED illumination. (b) Absorption spectrum of chlorophyll. (c) Two ROIs in the leaf were selected to access the spectral curves, which are plotted in (d). (e) Ratio of the 855 nm image to 659 nm image, which can be used as a chlorophyll distribution map of the leaf.

As shown in Fig. 7(c), a ROI was selected in the green area of the leaf and the corresponding reflection spectrum is drawn in Fig. 7(d). This spectrum shows an obvious red edge effect. For the yellow area, the absorption of red-light signal in 660 nm band was reduced due to the reduction of chlorophyll and the red edge effect was weakened. Accordingly, the leaf area rich in chlorophyll appeared green and its reflection spectral intensity had a local minimum in the 400 and 660 nm bands and increased sharply in the 660–800 nm bands. These results are shown in Fig. 7(c) and (d). Furthermore, the chlorophyll distribution map of the leaf (Fig. 7(e)) can be drawn by utilizing the image with low absorption (i.e., 855 nm) to divide into the image with high absorption (i.e., 659 nm). The size of the gray value in the figure is positively correlated with the content of chlorophyll in the leaf.

4. Conclusion

We have designed and manufactured a mobile multispectral imaging system and described its optical spectral–spatial characteristics in detail. The design information of the optical electromechanical system can be provided to interested researchers. The system utilized an LED matrix and industrial camera to realize multispectral imaging. The spectral resolution and spectral range was found to be dependent on the LED elements in the LED matrix. Herein, the LEDs we used cover 400–1100 nm, and the FWHM height of the optical spectra are all below 40 nm except for the 900–1000 nm band. The imaging region as well as the spatial resolution could be increased or decreased by replacing the imaging lens manually.

In addition, the imaging system can realize a wide range of applications. In our study, we applied the system to perform experiments on meat freshness, *in-vivo* imaging, and leaf chlorophyll analysis. Combined with the multispectral image data and the corresponding spectral analysis algorithm, we successfully achieved the classification of meat samples with different freshness, the localization of mouse tumor area, and the quantitative calculation of leaf chlorophyll spatial distribution. The spectral resolution of our multispectral imaging system was proved to be sufficient to realize accurate spectral numerical analysis. In contrast, unlike a hyperspectral camera, our multispectral imaging system can obtain spectral image data without spatial scanning, Therefore, the system can obtain high-definition spatial images in a shorter time.

CRediT authorship contribution statement

Fuzhou Shen: Software, Data curation, Formal analysis. **Hancheng Deng:** Resources, Investigation, Visualization. **Lejun Yu:** Methodology, Supervision, Resources. **Fuhong Cai:** Conceptualization, Supervision, Funding acquisition.

Declaration of Competing Interest

The authors declare that they have no known competing financial interests or personal relationships that could have appeared to influence the work reported in this paper.

Acknowledgment

This research is funded by Hainan Provincial Natural Science Foundation of China (2019RC080).

References

[1] R. Lu, B. Chen, Z. Cheng, P. Wang, RAFnet: Recurrent attention fusion network of hyperspectral and multispectral images, Signal Process. 177 (2020), 107737, https://doi.org/10.1016/j.sigpro.2020.107737.

[2] P.M. Pieczywek, J. Cybulska, M. Szymańska-Chargot, A. Siedliska, A. Zdunek, A. Nosalewicz, P. Baranowski, A. Kurenda, Early detection of fungal infection of stored apple fruit with optical sensors – Comparison of biospeckle, hyperspectral imaging and chlorophyll fluorescence, Food Control 85 (2018) 327–338, https://doi.org/10.1016/j.foodcont.2017.10.013.

[3] X. Hadoux, F. Hui, J.K.H. Lim, C.L. Masters, A. Pébay, S. Chevalier, J. Ha, S. Loi, C. J. Fowler, C. Rowe, V.L. Villemagne, E.N. Taylor, C. Fluke, J.-P. Soucy, F. Lesage, J.-P. Sylvestre, P. Rosa-Neto, S. Mathotaarachchi, S. Gauthier, Z.S. Nasreddine, J. D. Arbour, M.-A. Rhéaume, S. Beaulieu, M. Dirani, C.T.O. Nguyen, B.V. Bui, R. Williamson, J.G. Crowston, P. van Wijngaarden, Non-invasive in vivo hyperspectral imaging of the retina for potential biomarker use in Alzheimer's

disease, Nat. Commun. 10 (2019) 4227, https://doi.org/10.1038/s41467-019-12242-1.
[4] H. Aasen, A. Bolten, Multi-temporal high-resolution imaging spectroscopy with hyperspectral 2D imagers – From theory to application, Remote Sens. Environ. 205 (2018) 374–389, https://doi.org/10.1016/j.rse.2017.10.043.
[5] E. Kho, L.L. de Boer, K.K. Van de Vijver, F. van Duijnhoven, M.-J.-T.-F.-D. Vrancken Peeters, H.J.C.M. Sterenborg, T.J.M. Ruers, Hyperspectral Imaging for Resection Margin Assessment during Cancer Surgery, Clin Cancer Res. 25 (2019) 3572–3580, https://doi.org/10.1158/1078-0432.CCR-18-2089.
[6] E. VILLANUEVA, M. Gi. Julia, J.M.D. lo. Santos, I. Hervas, A. Navarro-GomezLechon, R. Rivera-Egea, N. Garrido, P–046 Application of hyperspectroscopy as a new sperm diagnostic and selection technique for ICSI based on hyperspectral signature of single spermatozoa – a proof of concept, Human Reproduction. 36 (2021). https://doi.org/10.1093/humrep/deab130.045.
[7] B. Lu, Y. He, Evaluating Empirical Regression, Machine Learning, and Radiative Transfer Modelling for Estimating Vegetation Chlorophyll Content Using Bi-Seasonal Hyperspectral Images, Remote Sensing. 11 (2019) 1979, https://doi.org/10.3390/rs11171979.
[8] N. Pahlevan, B. Smith, C. Binding, D. Gurlin, L. Li, M. Bresciani, C. Giardino, Hyperspectral retrievals of phytoplankton absorption and chlorophyll-a in inland and nearshore coastal waters, Remote Sens. Environ. 253 (2021), 112200, https://doi.org/10.1016/j.rse.2020.112200.
[9] D. Song, D. Gao, H. Sun, L. Qiao, R. Zhao, W. Tang, M. Li, Chlorophyll content estimation based on cascade spectral optimizations of interval and wavelength characteristics, Comput. Electron. Agric. 189 (2021), 106413, https://doi.org/10.1016/j.compag.2021.106413.
[10] T. Wang, F. Shen, H. Deng, F. Cai, S. Chen, Smartphone imaging spectrometer for egg/meat freshness monitoring, Anal. Methods 14 (2022) 508–517.
[11] F. Sigernes, M. Syrjäsuo, R. Storvold, J. Fortuna, M.E. Grøtte, T.A. Johansen, Do it yourself hyperspectral imager for handheld to airborne operations, Opt. Express. 26 (2018) 6021, https://doi.org/10.1364/OE.26.006021.
[12] J. Ning, Z. Xu, D. Wu, R. Zhang, Y. Wang, Y. Xie, W. Zhao, W. Ren, Compressive circular polarization snapshot spectral imaging, Opt. Commun. 491 (2021), 126946, https://doi.org/10.1016/j.optcom.2021.126946.
[13] P.N. Hedde, R. Cinco, L. Malacrida, A. Kamaid, E. Gratton, Phasor-based hyperspectral snapshot microscopy allows fast imaging of live, three-dimensional tissues for biomedical applications, Communications Biology. 4 (2021) 721, https://doi.org/10.1038/s42003-021-02266-z.
[14] H. Zhao, Z. Xu, H. Jiang, G. Jia, SWIR AOTF Imaging Spectrometer Based on Single-pixel Imaging, Sensors. 19 (2019) 390, https://doi.org/10.3390/s19020390.
[15] V. Batshev, A. Machikhin, A. Gorevoy, G. Martynov, D. Khokhlov, S. Boritko, V. Pozhar, V. Lomonov, Spectral Imaging Experiments with Various Optical Schemes Based on the Same AOTF, Materials. 14 (2021) 2984, https://doi.org/10.3390/ma14112984.
[16] J. Zhang, J. Li, Spectral shift correction and adaptive band selection for multispectral imaging, Opt. Lasers Eng. 144 (2021), 106632, https://doi.org/10.1016/j.optlaseng.2021.106632.
[17] C. Zeng, Y. Han, B. Liu, P. Sun, X. Li, P. Chen, Optical design of a high-resolution spectrometer with a wide field of view, Opt. Lasers Eng. 140 (2021), 106547, https://doi.org/10.1016/j.optlaseng.2021.106547.
[18] T.U. Kampe, The Compact Hyperspectral Prism Spectrometer: advanced imaging spectrometer for sustainable land imaging, in: Remote Sensing and Modeling of Ecosystems for Sustainability XV, SPIE, 2018: pp. 44–59. https://doi.org/10.1117/12.2322401.
[19] Z. Zhang, B. Hu, Q. Yin, T. Yu, S. Li, X. Gao, H. Zhang, Design of short wave infrared imaging spectrometer system based on CDP, Opt. Express. 23 (2015) 29758, https://doi.org/10.1364/OE.23.029758.
[20] M. Faraji-Dana, E. Arbabi, H. Kwon, S.M. Kamali, A. Arbabi, J.G. Bartholomew, A. Faraon, Hyperspectral Imager with Folded Metasurface Optics, ACS Photonics 6 (2019) 2161–2167, https://doi.org/10.1021/acsphotonics.9b00744.
[21] Y. Sun, Y. Wang, H. Xiao, X. Gu, L. Pan, K. Tu, Hyperspectral imaging detection of decayed honey peaches based on their chlorophyll content, Food Chem. 235 (2017) 194–202, https://doi.org/10.1016/j.foodchem.2017.05.064.
[22] Z. Sun, Z. Bu, S. Lu, K. Omasa, A General Algorithm of Leaf Chlorophyll Content Estimation for a Wide Range of Plant Species, IEEE Trans. Geosci. Remote Sens. 60 (2022) 1–14, https://doi.org/10.1109/TGRS.2021.3123117.
[23] H. Lee, W. Lee, H. Lee, S. Kim, M.V. Alban, J. Song, T. Kim, S. Lee, S. Yoo, Organic-Inorganic Hybrid Approach to Pulse Oximetry Sensors with Reliability and Low Power Consumption, ACS Photonics 8 (2021) 3564–3572, https://doi.org/10.1021/acsphotonics.1c01161.
[24] R. Liu, J.A. Winkelmann, G. Spicer, Y. Zhu, A. Eid, G.A. Ameer, V. Backman, J. Yi, Single capillary oximetry and tissue ultrastructural sensing by dual-band dual-scan inverse spectroscopic optical coherence tomography, Light Sci. Appl. 7 (2018) 57, https://doi.org/10.1038/s41377-018-0057-2.
[25] C. Tang, H. He, E. Li, H. Li, Multispectral imaging for predicting sugar content of 'Fuji' apples, Opt. Laser Technol. 106 (2018) 280–285, https://doi.org/10.1016/j.optlastec.2018.04.017.
[26] K. Wang, S. Wu, J. Zhao, M. Zhou, G. Li, D. Wang, L. Lin, Dual-mode spectrum of transmission and fluorescence using single ultraviolet LED light source and their application in analyzing total bilirubin in serum, Spectrochim. Acta Part A Mol. Biomol. Spectrosc. 264 (2022), 120305, https://doi.org/10.1016/j.saa.2021.120305.
[27] H. Liu, J. Sticklus, K. Köser, H.-J.-T. Hoving, H. Song, Y. Chen, J. Greinert, T. Schoening, TuLUMIS - a tunable LED-based underwater multispectral imaging system, Opt. Express. 26 (2018) 7811, https://doi.org/10.1364/OE.26.007811.
[28] X. Ma, X. Yuan, C. Fu, G.R. Arce, LED-based compressive spectral-temporal imaging, Opt. Express. 29 (2021) 10698, https://doi.org/10.1364/OE.419888.
[29] P.R. Yawale, V.G. Wagh, A.D. Shaligram, Impact of current controlled dimming on spectral characteristics of high power LEDs, Opt. Laser Technol. 115 (2019) 289–291, https://doi.org/10.1016/j.optlastec.2019.02.010.
[30] M.K. Barwar, L.K. Sahu, P. Bhatnagar, K.K. Gupta, A.H. Chander, A flicker-free decoupled ripple cancellation technique for LED driver circuits, Optik. 247 (2021), 168029, https://doi.org/10.1016/j.ijleo.2021.168029.
[31] T. Guo, M. Huang, Q. Zhu, Y. Guo, J. Qin, Hyperspectral image-based multi-feature integration for TVB-N measurement in pork, J. Food Eng. 218 (2018) 61–68, https://doi.org/10.1016/j.jfoodeng.2017.09.003.
[32] O. Okwuashi, C.E. Ndehedehe, Deep support vector machine for hyperspectral image classification, Pattern Recogn. 103 (2020), 107298, https://doi.org/10.1016/j.patcog.2020.107298.
[33] L. Gargani, C. Bruni, T. Barskova, V. Hartwig, M. Marinelli, M.G. Trivella, M. Matucci-Cerinic, A. L'Abbate, Near-infrared spectroscopic imaging of the whole hand: a new tool to assess tissue perfusion and peripheral microcirculation in scleroderma, Semin. Arthritis Rheum. 48 (2019) 867–873, https://doi.org/10.1016/j.semarthrit.2018.08.002.
[34] O. Seadia, D. Landesman-Milo, T. Kosoburd, N. Oren, L. Sherman, A. Yaniv, I. Landesman, Combined reflectance spectroscopy and coherent light backscattering measurement differentiate cervical cancer from normal epithelial tissue in a xenograft mouse model, Appl. Opt. 57 (2018) 8964–8970, https://doi.org/10.1364/AO.57.008964.